



NRL/FR/5674--12-10,219

All-optical, Three-axis Fiber Laser Magnetometer

G.A. CRANCH
G.A. MILLER
C.K. KIRKENDALL

*Fiber Optics Technology Branch
Optical Sciences Division*

April 16, 2012

Approved for public release; distribution is unlimited.

REPORT DOCUMENTATION PAGE

Form Approved
OMB No. 0704-0188

Public reporting burden for this collection of information is estimated to average 1 hour per response, including the time for reviewing instructions, searching existing data sources, gathering and maintaining the data needed, and completing and reviewing this collection of information. Send comments regarding this burden estimate or any other aspect of this collection of information, including suggestions for reducing this burden to Department of Defense, Washington Headquarters Services, Directorate for Information Operations and Reports (0704-0188), 1215 Jefferson Davis Highway, Suite 1204, Arlington, VA 22202-4302. Respondents should be aware that notwithstanding any other provision of law, no person shall be subject to any penalty for failing to comply with a collection of information if it does not display a currently valid OMB control number. **PLEASE DO NOT RETURN YOUR FORM TO THE ABOVE ADDRESS.**

1. REPORT DATE (DD-MM-YYYY) 16-04-2012		2. REPORT TYPE Formal Report		3. DATES COVERED (From - To) May 2011 to October 2011	
4. TITLE AND SUBTITLE All-optical, Three-axis Fiber Laser Magnetometer				5a. CONTRACT NUMBER	
				5b. GRANT NUMBER	
				5c. PROGRAM ELEMENT NUMBER 72747N	
6. AUTHOR(S) G.A. Cranch, G.A. Miller, and C.K. Kirkendall				5d. PROJECT NUMBER UW-747-021	
				5e. TASK NUMBER	
				5f. WORK UNIT NUMBER 6107	
7. PERFORMING ORGANIZATION NAME(S) AND ADDRESS(ES) Naval Research Laboratory 4555 Overlook Avenue, SW Washington, DC 20375-5320				8. PERFORMING ORGANIZATION REPORT NUMBER NRL/FR/5674--12--10,219	
9. SPONSORING / MONITORING AGENCY NAME(S) AND ADDRESS(ES) Office of Naval Research 1 Liberty Center 875 N. Randolph Street, Suite 1425 Arlington, VA 22203-1995				10. SPONSOR / MONITOR'S ACRONYM(S) ONR	
				11. SPONSOR / MONITOR'S REPORT NUMBER(S)	
12. DISTRIBUTION / AVAILABILITY STATEMENT Approved for public release; distribution is unlimited.					
13. SUPPLEMENTARY NOTES					
14. ABSTRACT This report describes the development of an undersea fiber-optic magnetometer, suitable for remote deployment as a moving target detection system. A comprehensive overview of the operating principle and performance of this sensor system is given. The magnetic field sensor utilizes the Lorentzian force acting on a current carrying bridge in the presence of a magnetic field, which drives its oscillation measured with a fiber laser strain sensor. The undersea node occupies a footprint of 303 mm × 303 mm and is connected to the opto-electronics unit through an undersea cable 1 km in length. The deployed orientation of the node is measured with an integrated MEMS inclinometer, which is optically powered. The sensor is capable of achieving a magnetic field resolution of 343 pT/Hz ^{1/2} at 1 Hz for 75 mA (rms) dither current when operated in a moderate vacuum of 1 kPa.					
15. SUBJECT TERMS Magnetometer Nonacoustic Fiber optic sensor Fiber laser sensor ASW					
16. SECURITY CLASSIFICATION OF:			17. LIMITATION OF ABSTRACT	18. NUMBER OF PAGES	19a. NAME OF RESPONSIBLE PERSON G.A. Cranch
a. REPORT Unclassified	b. ABSTRACT Unclassified	c. THIS PAGE Unlimited			SAR

CONTENTS

EXECUTIVE SUMMARY	E-1
1. INTRODUCTION	1
2. TRANSDUCER OPERATING PRINCIPLE AND PERFORMANCE.....	3
2.1 Minimum Detectable Magnetic Field.....	4
2.2 Mechanical Damping Mechanisms	4
2.3 Prototype Sensor Fabrication	5
2.4 Prototype Sensor Responsivity and Transducer Frequency Response.....	6
2.5 Inertial Sensitivity	7
2.6 Signal Frequency Response	8
2.7 Prototype Sensor Performance	8
2.8 Bias Coils	10
3. INTERROGATION TECHNIQUE AND DEMODULATION METHOD.....	11
3.1 Interferometric Decoding of Laser Frequency Shifts.....	11
3.2 Resonance Locking Technique	11
4. OPTICAL DELIVERY OF CURRENT DITHER	12
5. INCLINATION SENSOR	14
5.1 MEMS Inclinometer and Optical Powering Unit.....	15
5.2 All-optical Inclinometer	17
6. OPTICAL SYSTEM ARCHITECTURE FOR THREE-AXIS SENSOR SYSTEM.....	19
7. NODE DESIGN AND SENSOR INTEGRATION	20
8. PRELIMINARY SYSTEM EVALUATION AND FURTHER DEVELOPMENT	21
9. SUMMARY AND CONCLUSIONS	22
10. ACKNOWLEDGMENTS	23
REFERENCES	23
APPENDIX – Derivation of the Signal Frequency Response	23

FIGURES

Fig. 1 – Synthetic target signature in terms of Anderson functions.....	2
Fig. 2 – Lorentz force sensor operating principle	4
Fig. 3 – (a) Image of optical fiber soldered to ribbon and (b) prototype sensor	6
Fig. 4 – (a) Dependence of Q on ambient pressure for prototype sensor and (b) Noise spectral density of laser frequency modulation and Lorentz tone.....	9
Fig. 5 – Frequency response of prototype sensor.....	10
Fig. 6 – (a) Interferometric interrogation method for decoding fiber laser frequency shifts, (b) block diagram of signal processing, and (c) Labview front panel.....	12
Fig. 7 – (a) Optical delivery architecture of dither, (b) transfer characteristics of photonic power converter used for dither generation, and (c) noise spectral density of carrier noise.....	14
Fig. 8 – (a) MEMS inclinometer subsystem layout and (b) powering unit.....	16
Fig. 9 – (a) Core arrangement in multicore fiber and (b) multicore fiber inclinometer	17
Fig. 10 – (a) Difference in strain between two cores as a function of rotation for difference inclinations and (b) reported inclination vs. actual inclination for a bend angle of 120° and residual error.....	18
Fig. 11 – Optical architecture of a three-axis magnetometer	19
Fig. 12 – (a) Illustration of node layout and (b) fully instrumented node.....	20
Fig. 13 – Response of two axes to passing magnetic dipole, (a) dataset 1 and (b) dataset 2	21

EXECUTIVE SUMMARY

An undersea fiber optic magnetometer suitable for remote deployment as a moving target detection system has been developed and evaluated. This system fills a technology gap for permanently deployed, statically moored magnetometer arrays capable of wide-area coverage. Such systems can be used for coastline or harbor monitoring or for long-term monitoring in magnetic ranges.

Many technologies exist for measurement of magnetic field such as those based on SQUIDS, giant magnetoresistance (GMR), scalar resonance magnetometers, and flux-gates; however, a fiber optic sensor enables the field information to be encoded onto an optical carrier and transmitted over long distances without distortion or addition of noise. The chosen transduction mechanism, based on the Lorentz force, does not require cryogenic cooling or use of magnetic materials and provides an efficient means of coupling the signal to optical fiber as well as multiplexing information from multiple sensors. Furthermore, the use of vector field sensors provides three axes of field information for enhanced target detection methods such as remote referencing when compared to single-point measurements obtained from a scalar magnetometer. This is particularly important when the deployed sensor locality is in close proximity to non-uniform, man-made sources of magnetic noise. Such noise may affect primarily only one field axis and can be discarded during processing.

The sensors are incorporated into a pressure-resistant undersea node, which occupies a 303 mm × 303 mm footprint, and can be easily deployed from a small boat. The node is connected to an opto-electronics interrogation unit through an undersea cable that can be longer than 10 km. This greatly exceeds the standoff distances achieved with other magnetic field sensing technologies such as those based on flux gates and fiber optic magnetostrictive sensors. The deployed orientation of the node can be measured from inclination information obtained from an integrated microelectromechanical system (MEMS) inclinometer, and from bearing obtained from horizontal field components measured by the magnetometer.

A key component of the magnetic field sensor is a high-resolution fiber laser strain sensor. This encodes the magnetic field information onto an optical carrier, which is robustly transmitted over large distances (> 10 km) without signal distortion or degradation. The fiber laser sensor also enables information from multiple magnetic field sensors to be multiplexed onto a single optical fiber, providing an efficient means of sensor information transmission. The high strain resolution achieved by the fiber laser sensor technology enables this sensing approach to achieve the magnetic field measurement resolution and dynamic range necessary for target detection applications.

Incorporated alongside three orthogonal magnetic field vector sensors is an inclinometer, necessary to determine orientation of the remotely deployed node. An all-optical inclinometer, based on multicore fiber technology, has been evaluated for this purpose. Such a sensor is capable of matching the performance of conventional MEMS-based inclinometers, but can be operated over very long fiber lengths and requires no electrical power at the sensor head. Incorporation of such a sensor removes all electronics necessary for a conventional inclination sensor from the remote sensor node and dramatically reduces potential sources of local magnetic moment from magnetic materials and static electrical currents.

The simplicity of the sensor head maintains a low manufacture cost, which is important for large-scale arrays requiring high numbers of deployed sensors. The reported system is also suitable for integration with existing seabed-mounted fiber optic hydrophone arrays, providing a combined magnetic and acoustic sensing capability with a common optical multiplexing architecture.

ALL-OPTICAL, THREE-AXIS FIBER LASER MAGNETOMETER

1. INTRODUCTION

This report describes the development of an undersea fiber optic magnetometer suitable for remote deployment as a moving target detection system. A comprehensive overview of the operating principle and performance of this sensor system is given. The magnetic field sensor uses the Lorentz force acting on a current carrying bridge, which in the presence of a magnetic field drives its oscillation. The amplitude of the oscillation is measured with a fiber laser strain sensor mechanically coupled to the bridge. The high strain resolution achieved by fiber laser sensor technology enables this sensing approach to achieve the magnetic field measurement resolution and dynamic range necessary for target detection applications. The fiber laser sensor technology also provides an efficient means of multiplexing three sensors necessary for vector field measurement and transmitting sensor information over large distances without signal distortion or degradation.

The sensor is capable of achieving a magnetic field resolution of $343 \text{ pT/Hz}^{1/2}$ at 1 Hz for 75 mA (rms) dither current when operated in a moderate vacuum of 10^3 Pa . The field resolution is limited by thermo-mechanical noise arising from mechanical losses due to viscous air damping of the oscillator and represents a fundamental limit of performance. Improvement in sensitivity can be obtained by reduction in mechanical losses (achieved by further reducing the ambient pressure and removing residual internal oscillator losses) but at the expense of a reduced measurement bandwidth (currently 1 Hz).

The undersea node occupies a footprint of $303 \text{ mm} \times 303 \text{ mm}$ and is connected to the opto-electronics unit through an undersea cable 1 km in length. The deployed orientation of the node is measured with an integrated microelectromechanical system (MEMS) inclinometer, which is optically powered with an 810 nm laser diode and second photonic power converter. An optical inclinometer based on MCF is also evaluated and shown to match the performance of the MEMS inclinometer.

Detection of underwater targets by means of magnetic anomaly is a well-known concept. The steel mass of a surface ship or undersea vessel generates a magnetic field that is superimposed on the existing magnetic field of the Earth and modifies it slightly. One method to measure target-induced perturbations of the local magnetic field is commonly known as magnetic anomaly detection (MAD), where a fast moving (relative to the target) magnetometer is flown over the water surface. In such a system, searching for static magnetic anomalies with a moving magnetometer requires the use of magnetic gradiometers or scalar magnetometers (that measure total field amplitude). These magnetometers avoid the problem of large measurement errors that are generated in a moving vector sensor with varying attitude as well as (but less significantly) position [1].

An alternative method uses a statically mounted magnetic field sensor moored to the seabed, which measures the perturbation of the Earth's field caused by the target as it passes the sensor. Such a technique is known as moving target detection (MTD). In this configuration, analysis of data from multiple spatially dispersed sensing units enables remote referencing [1] to remove the drift due to temporal variation in the Earth's field as well as target tracking [2]. Such systems are suited to coastline or harbor monitoring and are the target applications for the current system.

The magnetic field of a submarine, \mathbf{B}_{sm} , is well represented by that of a magnetic dipole. If the z-axis of the reference coordinate system is aligned with the dipole moment, and the location of the magnetic origin properly selected, \mathbf{B}_{sm} takes the form,

$$\mathbf{B}_{sm}(r) = \frac{\mu_0}{4\pi} \left[\frac{3(\mathbf{M} \cdot \hat{r})\hat{r} - \mathbf{M}}{r^3} \right] \quad (1)$$

where \mathbf{M} is the magnetic dipole moment of the submarine or surface vessel, \mathbf{r} is the distance vector (\hat{r} is the corresponding unit vector), and μ_0 is the permeability of free space. It is assumed that the field is measured at some distance from the target, where higher order terms can be neglected. The strength of the magnetic field perturbation follows a $1/r^3$ dependence on range. The three components of the magnetic field due to the target measured at a distance \mathbf{r} are known as Anderson functions. An example of a typical synthetic target signature in terms of these functions is shown in Fig. 1. The coefficients making up these functions depend on the dipole strength and orientation, and the ship's velocity, heading, and distance from the magnetometer at the point of closest approach [3]. The problem of MTD is to measure these field transients in the presence of the ambient magnetic field.

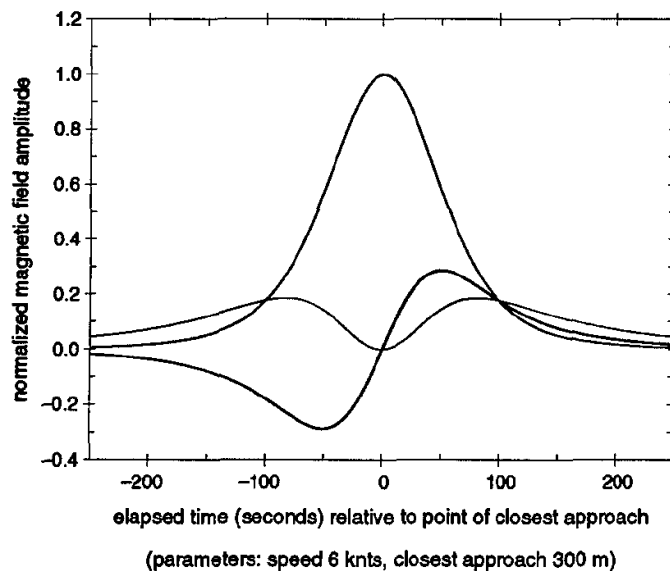


Fig. 1— Synthetic target signature in terms of Anderson functions. The magnetic dipole field of a submarine sailing at a constant velocity, as seen by a vector magnetometer at a fixed position, is always and in all its vector components, composed of a linear combination of three algebraic functions known as “Anderson functions.” Reprinted from Ref. 1.

Seabed-mounted sensors must be capable of stable, low-drift operation at very low frequency (< 1 Hz). Sensors may be operated autonomously for short-term (i.e., months) deployment or connected through a cable for permanent installation. The sensor system described herein addresses this latter requirement. For this program, the target specification for the magnetic field sensor is a field resolution of less than $1 \text{ nT/Hz}^{1/2}$ at 0.1 Hz, measurement range of 10^5 and measurement bandwidth of 1 Hz. The large measurement range is required to resolve the perturbation, which may be of order 1 nT, on the Earth's field, which may be in excess of $10 \mu\text{T}$.

For permanently installed arrays capable of wide-area coverage, a fiber optic cable provides a low-loss means of transmitting sensor data. A fiber optic sensor also provides compatibility with the information transmission medium. Such a sensor using magnetostrictive material as the transduction

medium was previously demonstrated [4]. Magnetostriction is used to convert an external magnetic field into strain within a transversely annealed Metglass ribbon around which optical fiber is wound. This is placed in one arm of an interferometer, which measures the strain induced in the optical fiber. The response of the Metglass to magnetic field is quadratic, such that by applying an AC magnetic dither field to the transducer (typically up to 20 kHz) the low frequency magnetic field of interest appears as modulation sidebands on a *carrier* at the dither frequency. However, magnetostrictive Metglass provides a far from ideal strain response. It has been observed that these materials can exhibit both a significant residual signal in the absence of a magnetic field, which can be equivalent to several μTesla as well as $1/f$ sideband noise [3]. Although methods based on choice of dither frequency and annealing conditions have been found to reduce these effects, it is generally necessary to operate the sensor closed-loop to overcome hysteresis in the magnetostrictive [5]. The fiber optic interferometer must also be quadrature locked in order to achieve sub- μradian phase resolution. For a three-axis magnetometer a total of four feedback loops are required, resulting in a relatively complex sensor head when the associated electronics for the feedback loops are integrated [1]. An array of eight three-axis magnetometers demonstrated magnetic field resolutions of $0.2 \text{ nT/Hz}^{1/2}$ at 0.1 Hz, limited by residual $1/f$ noise thought to be due to slow dynamic processes in the Metglass [6]. The need to provide electrical power and feedback signals to the sensor head is a significant disadvantage, particularly when the sensors are to be located several kilometers from the interrogation system.

These restrictions have led to the investigation of an alternative transduction mechanism. The current work uses the Lorentz force, which is a highly effective mechanism for magnetic field measurements. Its origin in the magnetic Coulomb force exerted between two moving charged particles results in a highly linear response that does not involve magnetic materials (i.e., magnetostriction) as a force mediator. Its behavior therefore does not depend on the magnitude of the local field and is not intrinsically limited in dynamic range. The magnitude of the force generated is proportional to the excitation current, enabling the sensitivity to be tailored for a specific operating range. Previous works have demonstrated promising results with the use of this transduction mechanism, albeit with rudimentary sensor implementations [7,8].

This report describes the development of a fiber optic magnetic field sensor based on the Lorentz force [9,10]. Three orthogonally mounted sensors have been integrated into a pressure tolerant housing with a two-axis MEMS inclinometer. The instrumented node is fully optically powered and connected to an interrogation unit through an undersea cable. This report describes the development of this system and is arranged as follows. The physical operating principles and the performance of a prototype sensor are described in Section 2. The interrogation and signal demodulation method are described in Section 3. Optical delivery of the dither signals is described in Section 4 and the inclination sensor and associated optical powering are described in Section 5. The optical architecture for the complete system is described in Section 6 and integration of the sensors into a custom designed pressure resistant node is discussed in Section 7. Finally, preliminary system evaluation, conclusions, and suggestions for further development and optimization are given in Sections 8 and 9.

2. TRANSDUCER OPERATING PRINCIPLE AND PERFORMANCE

A linear conductor carrying a current i in the presence of a magnetic field B acting orthogonal to its axis will experience a force per unit length given by $F_l = Bi$. The force acts in a direction orthogonal to both the charge flow and magnetic field. A time varying current, in the presence of a static magnetic field, will thus result in a time varying force. A sensor can be implemented by clamping the conductor at two points, forming an oscillating bridge. In the current sensor, oscillations of the bridge are measured with a high-resolution fiber optic strain sensor mechanically coupled to the bridge, illustrated in Fig. 2. The bridge exhibits a fundamental mechanical resonance typically in the range 200 to 400 Hz. At resonance, the amplitude of oscillation is increased by a factor equal to the mechanical quality factor of the oscillator relative to the oscillation amplitude at very low frequency. Operation of the transducer at resonance thus provides a significant increase in amplitude and hence responsivity of the sensor.

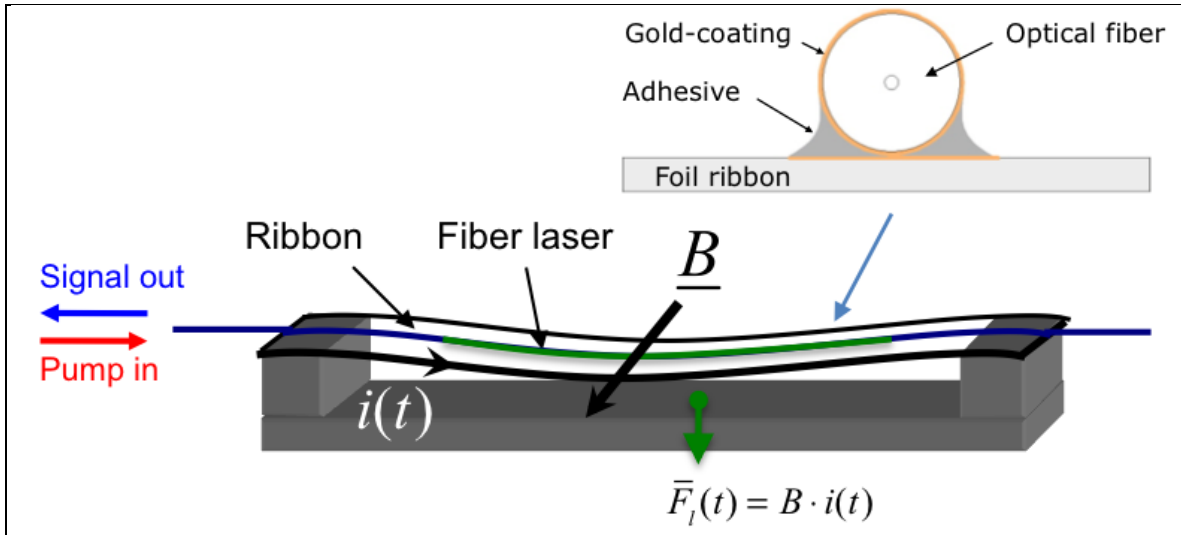


Fig. 2 – Lorentz force sensor operating principle. An aluminum ribbon with dimensions $50 \text{ mm} \times 3 \text{ mm} \times 50 \text{ }\mu\text{m}$ carries an ac current causing it to oscillate in the presence of a magnetic field, due to the Lorentz force. The oscillations induce axial strain in a fiber laser coupled to the ribbon, modulating its optical frequency.

2.1 Minimum Detectable Magnetic Field

The minimum detectable oscillation of the bridge at resonance is limited by fundamental thermo-mechanically induced oscillation of the bridge. It can be shown that in this regime the minimum detectable magnetic flux density is given by [11],

$$\delta B_m = \frac{(4k_B TR \Delta f)^{1/2}}{li} \quad (2)$$

where l is the bridge length, k_B is Boltzmann constant, T is the absolute temperature, Δf is the measurement bandwidth taken to be 1 Hz, and R is the mechanical loss of the oscillator. The mechanical loss is related to the mechanical quality factor by $Q = k_e / (\omega_r R)$, where k_e is the effective stiffness and $\omega_r = 2\pi f_r = (k_e / m_e)^{1/2}$. Here f_r is the lowest resonant frequency of the bridge. Utilizing a lumped mass model, the effective mass, m_e , for the fixed-fixed bridge is given by $m_e = (0.38)ml$, where m is the mass per unit length of the bridge. The minimum detectable field scales with $R^{1/2}$, therefore increasing the Q of the oscillator will improve the magnetic field sensitivity.

2.2 Mechanical Damping Mechanisms

There are several sources of mechanical loss in the oscillator, which contribute to the overall mechanical- Q . Studies of mechanical loss in micromechanical oscillators can be used to identify potential loss mechanisms in the present sensor [12]. An effective quality factor Q_{eff} can be obtained by summing the reciprocal of each contribution,

$$\frac{1}{Q_{eff}} = \frac{1}{Q_0} + \frac{1}{Q_{mount}} + \frac{1}{Q_{air}}, \quad (3)$$

where $1/Q_0$ is the intrinsic damping, $1/Q_{mount}$ is the clamping loss, and $1/Q_{air}$ is the viscous loss due to the surrounding medium. The intrinsic damping can be further separated into contributions from volume (i.e., material) loss, support loss, surface loss and thermoelastic loss (i.e., internal heating). Further discussion on these loss mechanisms can be found in Ref. 12.

The mechanical- Q of an oscillator in a viscous fluid with low viscosity (i.e., small dissipative effects) is given by [13],

$$Q_{fl} = \frac{\frac{4\mu}{\pi\rho b^2} + \Gamma_r(\omega_r)}{\Gamma_i(\omega_r)}, \quad (4)$$

where b is the width of the ribbon and ρ and μ are the density and viscosity of the surrounding fluid. $\Gamma(\omega)$ is the geometry dependent hydrodynamic function and the subscripts r and i denote real and imaginary parts. Expressions for $\Gamma(\omega)$ corresponding to the planar cantilever can be found in Ref. 13. For the case of air as the surrounding medium, the density is given by the ideal gas law, $\rho = (M/RT) \cdot P$, where M is the molar mass of the gas, R is the ideal gas constant, T is the temperature, and P is the ambient pressure.

2.3 Prototype Sensor Fabrication

In the prototype sensor, the conductor comprises a 50- μm thick aluminum ribbon. Mechanical clamps with a 50-mm spacing rigidly fix the ribbon to an aluminum housing. A fiber optic strain sensor is adhered to the top surface of the ribbon. Two methods have been developed to mechanically couple the optical fiber to the ribbon. One method uses a solvent-based adhesive and provides a thin interface between the two materials. A second method involves soldering the optical fiber to the ribbon and provides a more environmentally robust interface [14]. The soldering procedure involves multiple steps. A 3 mm wide ribbon with a narrow stripe of gold is formed using a lift-off patterning method. A 50 μm thick sheet of flat rolled, hard-tempered aluminum foil is spun coat with photoresist. A series of parallel stripes of titanium are then deposited, which provides adhesion for a layer of gold. Multiple ribbons are then laser cut from the aluminum sheet with the gold stripe centered. A precut solder preform is placed on the patterned ribbon and heated on a hot plate. The optical fiber is acid-stripped, providing a pristine surface onto which titanium and gold are evaporated evenly, yielding a coating thickness approximately 300 nm. The attachment process involves holding the fiber under tension while in contact with the heated solder stripe. The aim of this procedure is to define a minimal meniscus cross-section between the fiber and stripe on the ribbon. An illustration of the composite beam is shown in the inset of Fig. 2. The metal coated fiber is located along the center of the aluminum ribbon and the solder occupies a strip approximately 0.5 mm in width. An image of the composite ribbon is shown in Fig. 3(a). Once assembled, the ribbon and optical fiber are mounted into a sensor housing. The ribbon is held under tension and positioned onto the base of the housing. Two custom designed clamps provide a precise fixed edge support to the tensioned ribbon. One clamp is electrically isolated from the housing with a mica sheet, enabling the dither current to be applied to the ribbon. The optical fiber exits from each end of the housing through a furcation tube. Induction coils are also positioned on either side of the ribbon center. These allow a calibration signal or bias field to be applied to the transducer. Electrical connections exit the housing through a feed-through to an external connector. A cover is placed over the housing base,

yielding a sensor with dimensions 100 mm × 37 mm × 25 mm. Nonmagnetic materials (aluminum and plastic) are used wherever possible within the sensor housing.

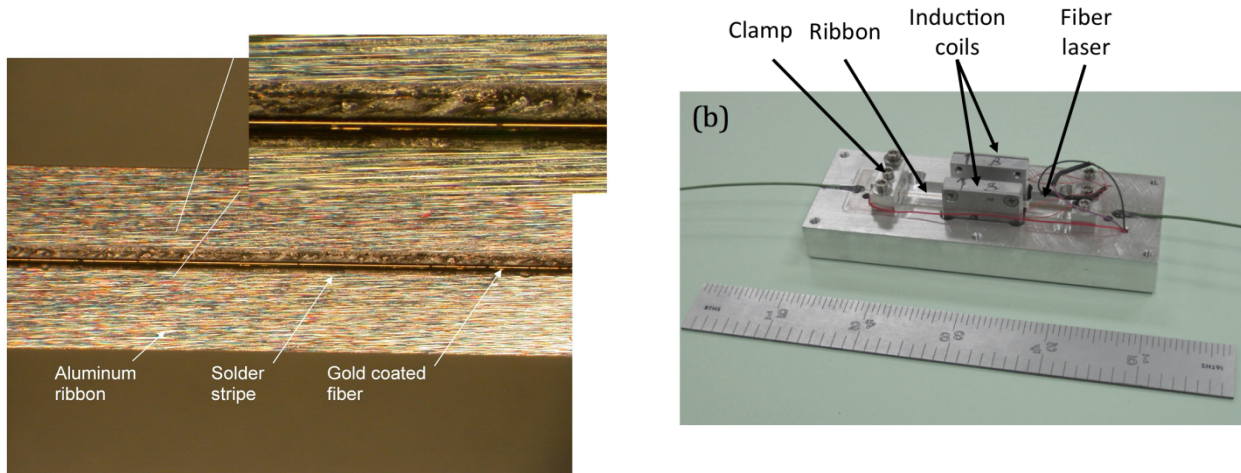


Fig. 3 – (a) Image of optical fiber soldered to ribbon and (b) prototype sensor

A design strategy to minimize sources of internal loss has been adopted. The material constituents of the composite ribbon have been reduced to metal and glass only. A soft polymer coating often applied to optical fiber is removed and replaced with a vacuum deposited coating of gold. This acts as a hermetic seal and also permits soldering as an adhesion method between the optical fiber and ribbon. The clamps, ribbon and aluminum support housing are precision machined to minimize losses due to defects and ensure oscillation occurs in a single preferential direction (i.e., perpendicular to the plane of the ribbon). This also ensures that motion in the plane of the ribbon is minimized, which reduces cross-axis sensitivity. This is very important for accurate measurement of vector fields with large differences in amplitude between orthogonal field components. Values of mechanical- Q obtained for a sensor with solder adhesion are comparable to those using solvent based adhesive.

2.4 Prototype Sensor Responsivity and Transducer Frequency Response

The fiber optic strain sensor comprises a fiber laser sensor. Oscillations of the ribbon induce flexural strain within the core of the optical fiber, which modulates the emission frequency of the fiber laser. This forms a robust method of transporting the signal information over long fiber lengths independent of optical power and variation in transmission losses through the system. The fiber laser strain sensor is capable of resolving axial length fluctuations less than $1 \text{ fm/Hz}^{1/2}$ at 1 kHz, approximately two orders of magnitude higher than achieved with fiber optic interferometry [15]. Since the laser can support large frequency modulations, the dynamic range of the measurement is also large (greater than $\sim 120 \text{ dB/Hz}$) limited ultimately by the electronic sampling rate. The fiber laser sensor is formed by two Bragg gratings, separated by a few centimeters, written into an erbium-doped optical fiber. The doped fiber is spliced between two passive fibers, which deliver the 980 nm pump radiation generated from a laser diode. The laser emits a single frequency around 1550 nm.

When operated at the mechanical resonance, the resolution achieved by the fiber laser sensor is adequate to resolve the thermo-mechanically induced bridge oscillations. The frequency shift of the fiber laser emission is calculated from the flexural strain induced in the core of the optical fiber, weighted by

the spatially varying laser mode shape, and integrated over the length of the ribbon. A simplified approximate expression for the response of the sensor can be obtained by assuming the ribbon is tension-free and the laser mode is tightly confined to the center of the bridge (corresponding to an ideal distributed feedback fiber laser). The laser frequency shift, $\Delta\nu_s$, due to a change in the magnetic flux density, ΔB , and current, i , is given by [11],

$$\frac{\Delta\nu_s}{\nu_s} = (0.78) \frac{d_n l^2 i}{24EI} \Delta B, \quad (5)$$

where ν_s is the laser frequency, EI is the product of the effective Young's modulus and moment of inertial of the composite ribbon, d_n is the distance of the optical fiber core to the neutral surface, and the factor of 0.78 accounts for the stress-optic effect. For a harmonically varying current the dynamic motion of the ribbon is accurately described by the equation for a one-dimensional, viscously damped harmonic oscillator driven by a sinusoidal force, $f_0 \sin(\omega t)$, given by

$$m_e \ddot{y} + R\dot{y} + k_e y = f_0 \sin(\omega t), \quad (6)$$

where \dot{y} represents differentiation with respect to time, m_e and k_e are the effective mass and stiffness of the ribbon and fiber and R is the mechanical loss. Equation (6) can be solved to yield the relative displacement between the ribbon and rigid supports, $Z(\omega)$, yielding,

$$|Z(\omega)| = (f_0 / k_e) \cdot \left(\left[1 - (\omega / \omega_r)^2 \right]^2 + (\omega / \omega_r)^2 / Q^2 \right)^{-1/2} \quad (7)$$

and

$$\arg(Z) = \tan^{-1} \frac{(1/Q)(\omega / \omega_r)}{1 - (\omega / \omega_r)^2}. \quad (8)$$

Defining the normalized displacement as $\hat{Z}(\omega) = Z(\omega) / (f_0 / k_e)$, the frequency-dependent responsivity of the sensor can be represented using Eq. (7) by $\Delta\nu_s / \nu_s \cdot |\hat{Z}(\omega_d)|$ where ω_d is the dither angular frequency. If the dither frequency is set to the bridge resonance, then $\hat{Z}(\omega_d)$ reduces to $\hat{Z}(\omega_r) = Q \exp(-j\pi/2)$, where $j = \sqrt{-1}$. In this case, the laser frequency shift can be expressed as

$$|\Delta\nu_s(\omega_r)| \propto i(\omega_r) \cdot Q \cdot \Delta B, \quad (9)$$

where $|\Delta\nu_s(\omega_r)|$ is the amplitude of the laser frequency modulation at the resonant frequency, ω_r .

2.5 Inertial Sensitivity

Any motion of the sensor housing that generates oscillations of the bridge at the resonant frequency will be indistinguishable from the magnetic field signal and thus reduce the sensor resolution. Therefore, the response of the bridge to support motion is an important performance characteristic. The inertial force is given by $F_i = \eta \ddot{y}$, where η is the mass per unit length of the bridge. The ratio of the magnetically

induced force, F_l , to the inertial force acting in a plane perpendicular to the bridge is a figure of merit for the sensor and should be made as large as possible (i.e., ideally, the bridge should have no mass).

2.6 Signal Frequency Response

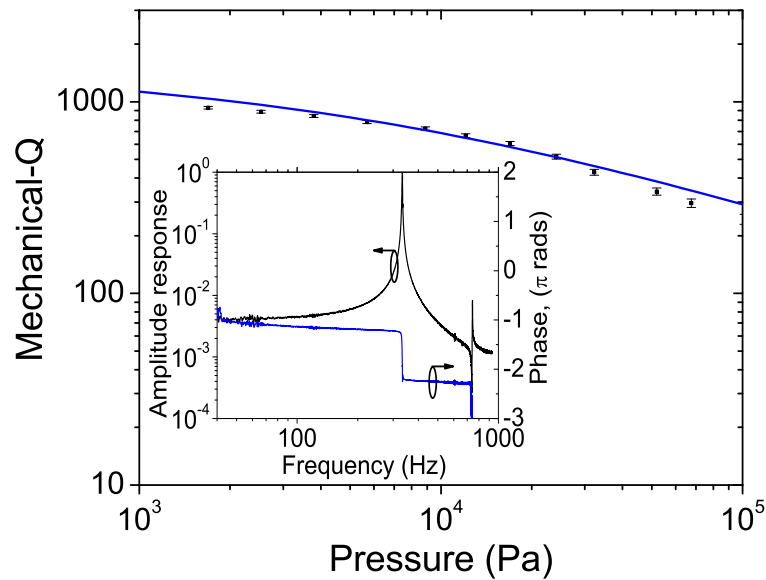
When the sensor is operated at its mechanical resonance for highest sensitivity, it is unsuited to measurement of transient signals, which will cause the oscillator to ring. The high- Q of the oscillator restricts the sensor's ability to measure magnetic field to low frequencies (< 1 Hz). However, this is adequate for the target application. The complex signal frequency response of the sensor, $\hat{R}(f_B)$, when operated at resonance is derived in Appendix A and is shown to be

$$\hat{R}(f_B) = \left(1 + \left(\frac{2Qf_B}{f_r}\right)^2\right)^{-\frac{1}{2}} \exp\left(-j \cdot \tan^{-1}\left(\frac{f_r}{2Qf_B}\right)\right), \quad (10)$$

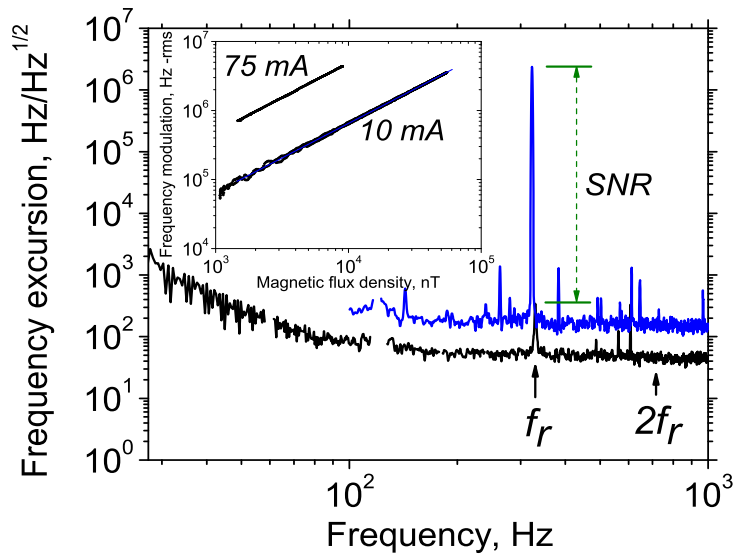
where f_B is the Fourier frequency of the magnetic field.

2.7 Prototype Sensor Performance

The frequency response of the transducer is characterized by placing it within a known magnetic field and sweeping the frequency of the dither current. The frequency modulation of the laser is recorded as a function of dither frequency. A typical frequency response is shown in the inset of Fig. 4(a), indicating a fundamental resonance of 322 Hz with an overtone at 740 Hz. The operating point of the sensor is at the fundamental resonance. The dependence of Q on ambient pressure is shown in Fig. 4(a). This is found to increase in proportion to $P^{-1/2}$ for decreasing pressure to 10^4 Pa. Below 10^4 Pa, the pressure dependence decreases significantly. The Q is shown to increase from $244 \pm 4\%$ at ambient pressure to $931 \pm 4\%$ at a reduced pressure of 1700 Pa. The theoretical trace is also shown, calculated by assuming a residual Q of 1800 and combining this with Q_{air} , according to Eq. (4). The dynamic viscosity of air is taken to be $\mu = 1.81 \times 10^{-5}$ Pa.s at 298 K. The experimental measurement and theory are in close agreement indicating that viscous air damping is dominant at ambient pressure. It can be concluded that viscous air-damping dominates all damping mechanisms at ambient pressure and represents a limiting factor to the magnetic field resolution of the sensor [16]. Sealing the sensor within a vacuum to increase the Q is possible, which would also lead to an increase in the magnetic field resolution according to Eq. (2); however, this comes at the expense of a reduced measurement bandwidth according to Eq. (10).



(a)



(b)

Fig. 4 – (a) Dependence of Q on ambient pressure for prototype sensor (in this sensor the optical fiber is adhered to the ribbon with a solvent based adhesive – the result is expected to be similar for the soldered ribbon). (Inset) Frequency response of transducer, and (b) Noise spectral density of laser frequency modulation and Lorentz tone. The noise spectrum in units of $\text{Hz}/\text{Hz}^{1/2}$, shown by the black trace, is measured by placing the sensor in an environmentally isolated chamber with no excitation current applied. The Lorentz tone generated with an excitation current of 75 mA (rms) and flux density of $2.4 \mu\text{T}$ is shown by the blue trace (note that a factor of 2 has been applied to this data to offset from the noise data). (Inset) Frequency modulation response of the fiber laser, $\Delta\nu$, to a static magnetic field, ΔB , measured by placing the sensor in a known magnetic field, generated by a Helmholtz coil, and calibrating relative to a Hall probe for the specified excitation current. A least square linear fit is plotted through the 10 mA dataset, indicating a correlation coefficient of 0.99988.

The dependence of the laser frequency modulation, $\Delta\nu_s$, on magnetic flux density, ΔB , is shown in the inset of Fig. 4(b) for excitation currents of 10 mA and 75 mA(rms). Their relationship is shown to exhibit excellent linearity in accordance with Eq. (5). The slope of the measured data indicates a responsivity of $6.5 \text{ Hz/nT/mA} \pm 10\%$ measured at ambient pressure. Fig. 4(b) also shows the laser frequency noise when the excitation current is removed and the sensor is placed in an environmentally isolated chamber. A peak is observed in the laser frequency spectrum at the beam resonance, indicating the presence of residual beam deflection in the absence of any applied signal. The peak exceeds the self-noise of the fiber laser by a factor of 6.5 and imposes a limit on the minimum detectable magnetic induction. According to Fig. 4(b), the frequency noise $\delta\nu$ at f_r , in the absence of excitation, is $343 \text{ Hz/Hz}^{1/2}$, yielding a measurement resolution of $53 \text{ (nT.mA)/Hz}^{1/2}$ or $704 \text{ pT/Hz}^{1/2}$ for 75 mA (rms) excitation current. The increase in Q attained by operating the sensor at a reduced pressure of 1700 Pa would yield a measurement resolution of $360 \text{ pT/Hz}^{1/2}$ at 1 Hz with 75 mA of excitation current. Figure 4(b) also shows the signal (known as the *Lorentz* tone) generated for an excitation current of 75 mA(rms) and magnetic flux density of $2.4 \text{ } \mu\text{T}$, yielding a signal-to-noise ratio (SNR) of 71 dB.

The signal frequency response of the sensor is characterized by applying a harmonically varying magnetic field and measuring the sensor output as a function of frequency for constant magnetic field amplitude. The result is shown in Fig. 5. The sensor response is found to decrease by a factor of 0.5 at 1 Hz. Also shown is the theoretical response according to Eq. (10), which is in close agreement with the measured response. Increasing Q to 931 causes the frequency response to fall to 0.13 at 1 Hz.

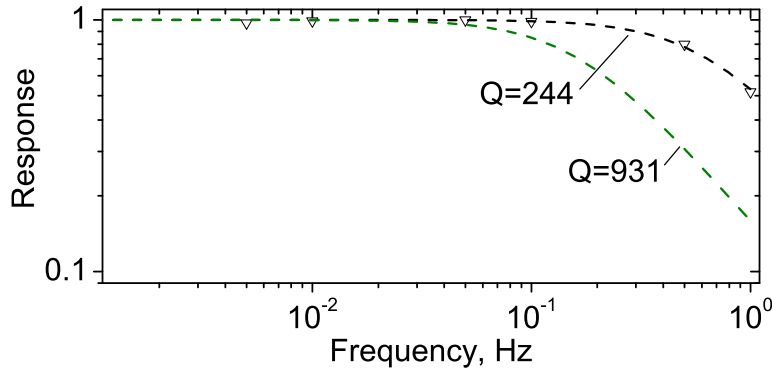


Fig. 5 – Frequency response of prototype sensor (open triangles are experimental measurement and dotted lines are theory according to Eq. (10)).

2.8 Bias Coils

Two toroidal induction coils are located on either side of the center of the ribbon. The coils are potted inside aluminum enclosures using a thermal compound to provide heat dissipation. They are connected in series to form a Helmholtz coil and enable a controllable magnetic field to be applied to the ribbon. This additional field can either be used for calibration purposes or to apply a bias field. A bias field reduces the local static field acting on the ribbon. This eases the dynamic range requirement of the sensor as the total

field acting on the ribbon, and hence the Lorentz tone amplitude, is reduced.¹ Assuming the bias field is sufficiently stable, the ambient perturbations associated with the target will be unaffected by the bias field. The current for the bias field can be optically supplied using the same technique for the dither current described in Section 4. The effect of a bias field on adjacent magnetometers requires further investigation.

3. INTERROGATION TECHNIQUE AND DEMODULATION METHOD

3.1 Interferometric Decoding of Laser Frequency Shifts

Laser frequency shifts are decoded by converting them into an intensity modulation using an imbalanced fiber optic interferometer. The basic optical arrangement for a fiber laser sensor is illustrated in Fig. 6(a). The fiber laser sensor is optically pumped at 980 nm with a semiconductor laser diode. The output of the laser diode is coupled to a single-mode fiber through a wavelength division multiplexer (WDM). The physical separation between the pump diode and laser may be several kilometers, and isolators are used to prevent Rayleigh scattering entering the laser cavity. The output of the fiber laser is carried through the same fiber and injected into an imbalanced Michelson interferometer. Each arm of the Michelson interferometer is terminated with a Faraday rotation mirror to prevent polarization induced signal fading. Interferometric decoding techniques have been demonstrated to achieve strain resolution limited by fundamental frequency fluctuations of the fiber laser and the ability to resolve displacements in the laser cavity less than $1 \text{ fm/Hz}^{1/2}$ at 1 kHz [15]. A method known as phase-generated carrier (PGC) is used to extract and track the interferometric phase [17]. This technique provides the most accurate measurement of interferometric phase, however, its implementation requires very high sampling rates ($\sim 500 \text{ kSamples/s}$ per sensor).

The signal processing steps are illustrated as a flow chart in Fig. 6(b) and were implemented in Labview. The magnetic signal appears as a tone (i.e., the Lorentz tone) in the interferometric phase at the dither frequency with an amplitude proportional to the magnetic flux density, as illustrated in Fig. 4(b). A signal proportional to the output current from the photodiode, i_{ph} , is injected into the PGC demodulator. This generates the sin and cosine of the interferometric phase ϕ and incorporates a fringe counter to track the phase order. An amplitude demodulator (AM demod) extracts the amplitude of the magnetic field tone by synchronous detection with the dither signal. The Labview program is capable of interrogating three sensors simultaneously.

3.2 Resonance-locking Technique

Thermal fluctuations in the sensor head can cause the mechanical resonance frequency to shift causing severe drift in the measurement as the resonant frequency ω_r deviates substantially from the dither frequency ω_d . This problem can be overcome if the dither frequency is allowed to track the mechanical resonance. The frequency response of the transducer (not to be confused with the signal frequency response shown in Fig. 5) undergoes a π phase change about the resonant frequency (shown in the inset of Fig. 4(a)). This phase shift is also observed in the phase of the Lorentz tone and provides a suitable error signal to lock to the mechanical resonance. The set point for this phase difference between the dither signal and Lorentz tone corresponds to the peak of the mechanical resonance (i.e., ω_r) and is determined during an initial calibration procedure. Referring to Fig. 6(b), a phase comparison (Phase comp) is performed between the Lorentz tone and dither signal, $\sin(\omega_d t)$, and a correction signal is generated and fed back to the frequency of the dither, locking it to the mechanical resonance.

¹ The bias field should not null the total field, as the resonance locking method, described in Section 3.2, requires a small non-zero field to operate.

All signals are generated and processing performed within Labview 8.5 and an illustration of the front panel is shown in Fig. 6(c).

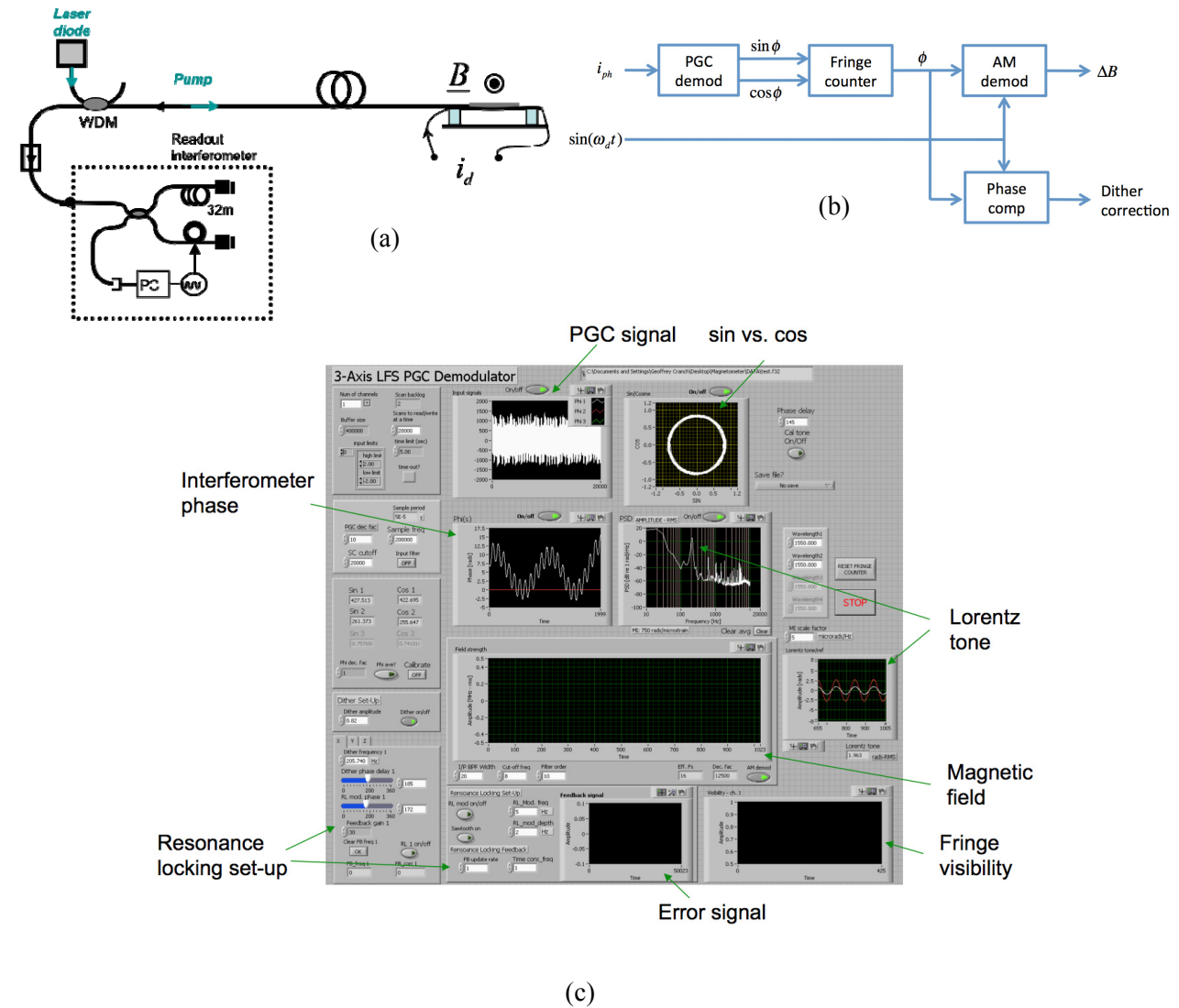


Fig. 6 – (a) Interferometric interrogation method for decoding fiber laser frequency shifts, (b) block diagram of signal processing, and (c) Labview front panel

4. OPTICAL DELIVERY OF CURRENT DITHER

The dither current is delivered to the sensor head through a dedicated single-mode optical delivery fiber [18]. Light from a laser diode is transmitted through the delivery fiber and converted into a current with a photovoltaic converter, as illustrated in Fig. 7(a). Polarization dependence of the photovoltaic converter responsivity gives rise to current fluctuations, which can be minimized by depolarizing the optical signal. The outputs of two 1480 nm laser diodes are polarization multiplexed onto a single fiber using a polarization maintaining combiner (PMC), producing a depolarized optical signal. The laser diodes are current modulated by the dither signal (this is generated within Labview and output to a D/A channel). The dither signal is a square wave at the dither frequency. Use of such a signal instead of

sinusoidal modulation avoids problems associated with variation in the laser diode slope efficiency with injection current and nonlinearity in the response of the optical converter. The photovoltaic converter, known as a photonic power converter (PPC),² consists of a planar array of photodiodes connected in series and operated in a photovoltaic mode. This enables high current generation into a low impedance load. The transfer characteristic of the PPC is shown in Fig. 7(b). Here, the DC current generated is shown as a function of incident power for load impedances in the range of 1 Ω to 9 Ω . In the linear regime, the response is 0.75 A/W and saturates at an optical power dependent on the load impedance. For a load impedance of 1 Ω , saturation occurs at 300 mW, falling to \sim 70 mW at 9 Ω . The saturation of the response is advantageous and can be used as a current limiter. Fluctuations in the dither current translate directly to fluctuations in the sensor output, according to Eq. (9), and thus can be a source of measurement error. When the PPC is operated in the saturated regime, the conversion of power fluctuation to current fluctuation is reduced by a factor inversely proportional to the slope of the response curve and is therefore an ideal operating regime.

The sideband noise of the dither current generated by the PPC using this method has been characterized by measuring the voltage noise across the load resistor. The single sided power spectral density of current fluctuation about the dither frequency (\sim 300 Hz) is shown in Fig. 7(c) for two voltage levels. For the case of 0.1 V, the noise spectral density is -86 dB/Hz at 1 Hz and reduces to -104 dB/Hz for a voltage of 1 V due to the detector saturation (the higher voltage corresponds to either higher incident power or higher load impedance). The dither current noise can be directly related to the magnetic field resolution. For example, in the presence of a background field of 10 μ T, a current noise of -100 dB/Hz limits the field resolution to 0.1 nT/Hz^{1/2}.

One disadvantage of optical delivery of the dither signal in the implementation described above is that the photocurrent does not vary about zero. For a time varying current of the form,

$$i(t) = \begin{cases} 0 & \text{for } 0 < t < a/2 \\ i_{pk} & \text{for } a/2 < t < a \end{cases}, \quad (11)$$

where i_{pk} is the peak amplitude, a is the period of the square wave and $\omega_d = 2\pi/a$, the Fourier series is

$$i_{fs}(t) = i_{pk} \left\{ \frac{1}{2} - \frac{2}{\pi} \left(\cos \omega_d t - \frac{1}{3} \cos 3\omega_d t + \frac{1}{5} \cos 5\omega_d t - \dots \right) \right\}. \quad (12)$$

The dither current therefore comprises a DC component with amplitude $i_{pk}/2$ as well as the desired component at ω_d with odd harmonics. The DC component produces a current loop, which generates its own magnetic field and is highly undesirable for DC magnetic field measurement. The effect of this current loop is minimized in the present system by use of twisted pair electrical connections. One possible method to suppress this DC term is to launch a second optical signal with an inverted modulation and detect with a second PPC. The difference between the two PPCs will be a current oscillating about zero, hence suppressing the DC term in Eq. (12). However, the disadvantage of this implementation is the need for an additional optical signal and PPC. An alternative solution may be to add a DC blocking capacitor to the existing PPC output to prevent the DC current from passing through the sensors.

² Photovoltaic power converters, www.jdsu.com

According to Fig. 7(b), the present system can provide a current of 250 mA for ~ 400 mW of optical power at a load impedance of 1Ω . This yields a dither current of $(2/\pi)*250 / \sqrt{2} = 113$ mA (rms) for one sensor or ~ 38 mA (rms) for three sensors.

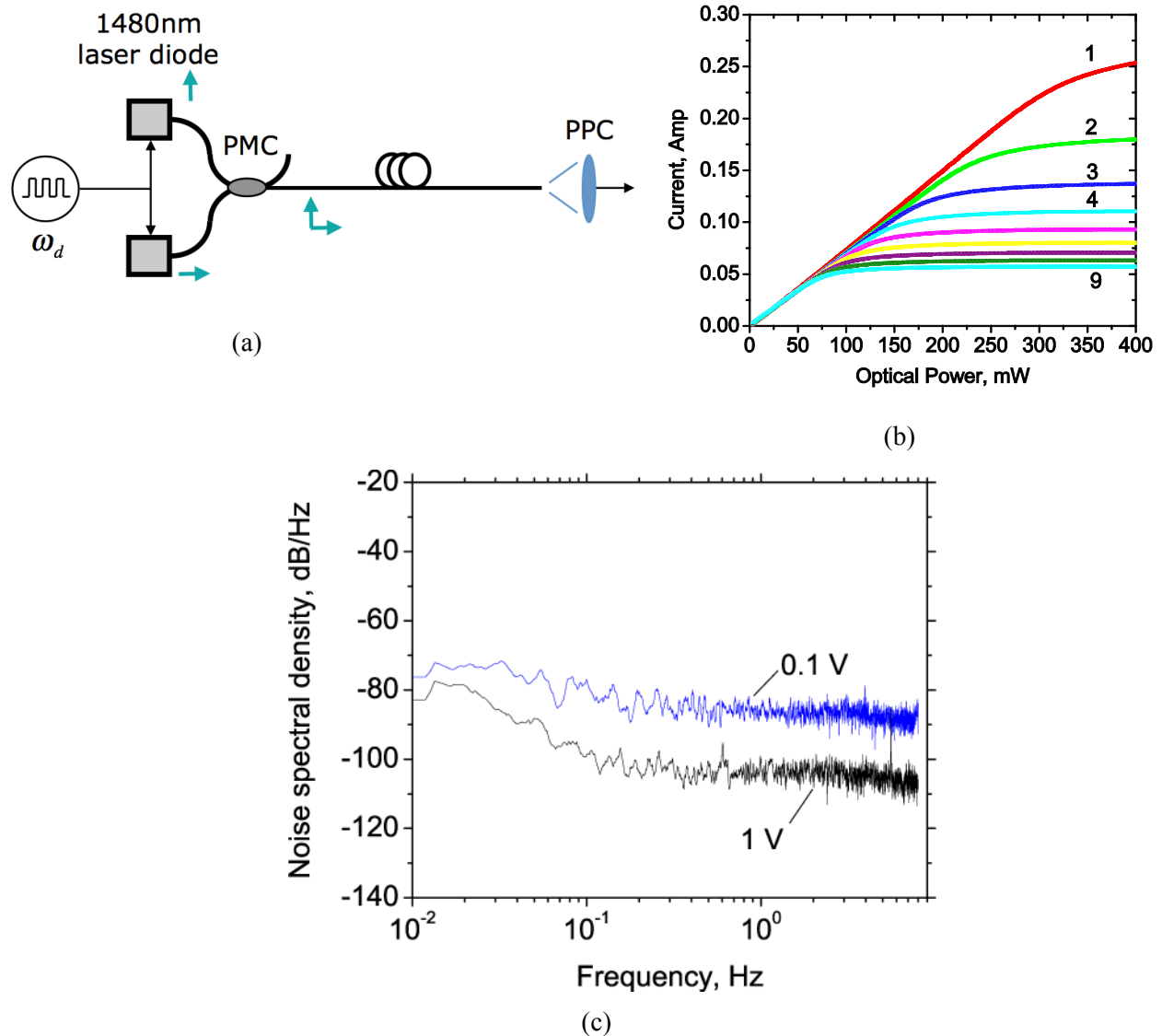


Fig. 7 – (a) Optical delivery architecture of dither, (b) transfer characteristics of photonic power converter used for dither generation for increasing low impedance in ohms, and (c) noise spectral density of carrier noise.

5. INCLINATION SENSOR

The orientation of a remotely deployed undersea magnetometer is generally unknown. For land based magnetic field measurements, the vector magnetometer is (manually) oriented to a predefined reference frame (such as magnetic north). For remotely deployed sensors, a means of projecting the three orthogonal measurements made by the magnetometers onto a common reference frame is required. This procedure is mathematically equivalent to a projection of one basis set onto another rotated version in

three dimensions. In a three-axis sensor, this projection requires knowledge of the two-dimensional inclination of the vector magnetometers. The transformed data combined with the bearing of the horizontal vector components relative to magnetic north for each three-axis sensor is sufficient to reference multiple spatially separated three-axis magnetometers.

5.1 MEMS Inclinometer and Optical Powering Unit

The inclination is obtained with a commercially available MEMS inclinometer (SignalQuest, SQ-S12X-360DA). Such a device requires several mA of electrical power at 2.9 V supply voltage. This power is supplied optically using an additional PPC configured for electrical power delivery. The optical power for this PPC is generated by an 810 nm laser diode (capable of generating up to 2 W) coupled to a multimode fiber. The output of the PPC charges a capacitor bank, supplying a constant power to the MEMS inclinometer (this subsystem is illustrated in Fig. 8(a)). The MEMS power can also be enabled remotely by a separate optical control signal. The output of the MEMS inclinometer is a digital serial packet encoded with the inclination readings. The digital signal is used to modulate an 850 nm VCSEL coupled to a multimode fiber, which is also powered from the capacitor bank, to relay the inclination information back to the interrogation unit. The circuit board is shown in Fig. 8(b). The resolution of the inclinometer is 0.1° , accuracy $\pm 2^\circ$ with an inclination range of 360° and 180° in the x- and y-axis, respectively.

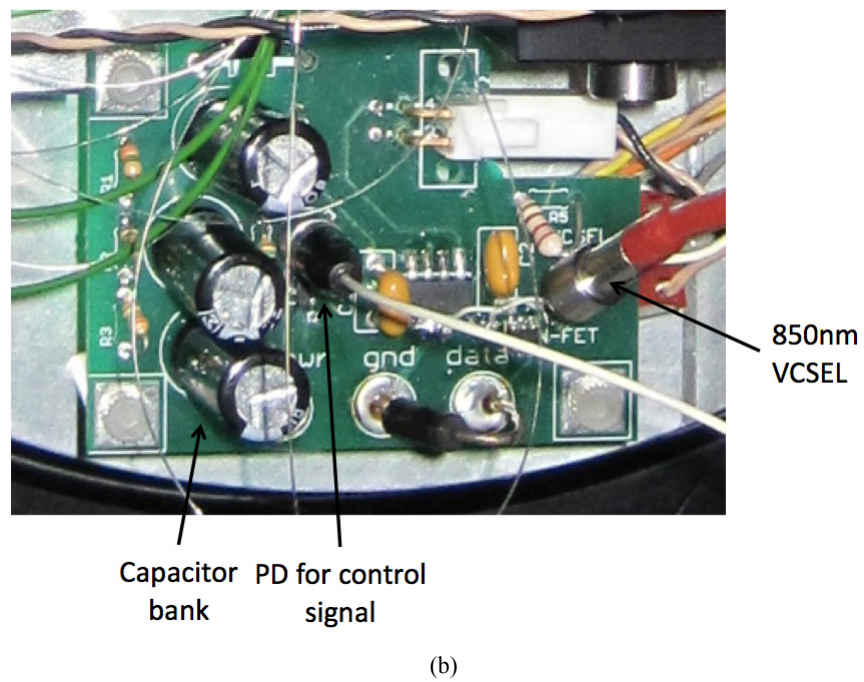
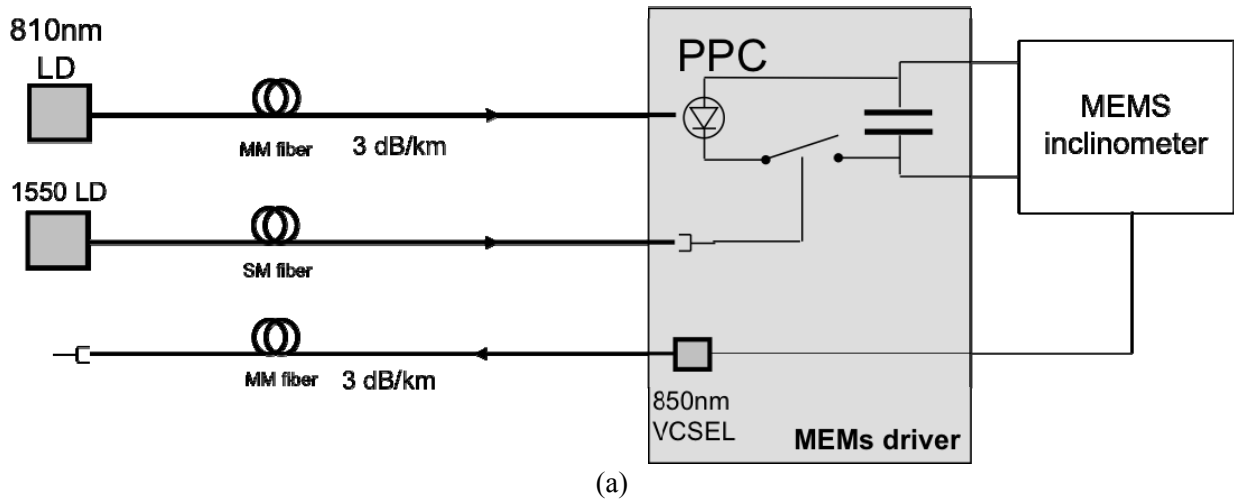


Fig. 8 – (a) MEMS inclinometer subsystem layout and (b) powering unit

5.2 All-optical Inclinometer

An all-optical inclinometer has also been investigated as a potential replacement for the MEMS inclinometer. The inclinometer is based on a multicore optical fiber (MCF) with four single-mode cores (illustrated in Fig. 9(a)). When the fiber is bent, the cores experience elongation or contraction, due to flexure strain [19], depending on their position relative to the neutral surface and orientation to the bending direction. The strain is measured with fiber Bragg gratings, which are written into each core using an ultraviolet laser. Measurements of the differences in induced strain between the FBGs enables bending in two dimensions to be resolved. An inclinometer is formed by supporting the MCF as a cantilever in a vertical orientation. A prototype sensor is illustrated in Fig. 9(b). When subject to tilt, bending of the optical fiber due to gravity enables the inclination of the fiber support to be determined. Calibration is performed by applying a known inclination to the housing and measuring the difference in strain experienced by two opposing cores, while rotating the housing. This is repeated for multiple inclinations. The difference in strain between two FBGs as a function of rotation for three inclination angles of 9° , 45° , and 81° is shown in Fig. 10(a). The FBG strain is measured using an interferometric method, and as such, the difference in strain is reported as a difference in phase [20]. The reported inclination vs the actual inclination is shown in Fig. 10(b) for the case of a bend angle of $\theta_a = 120^\circ$. Also shown in Fig. 10(b) is the measurement residual indicating an error of $\pm 0.1^\circ$.

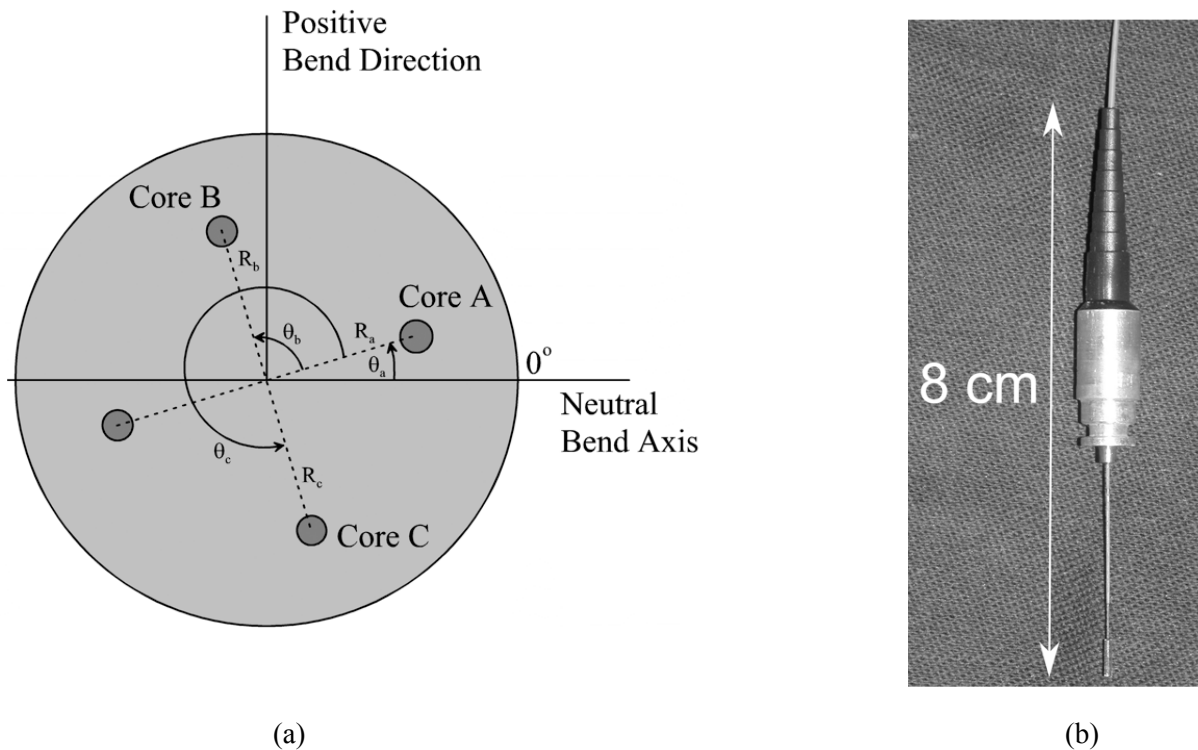


Fig. 9 – (a) Core arrangement in multicore fiber and (b) multicore fiber inclinometer

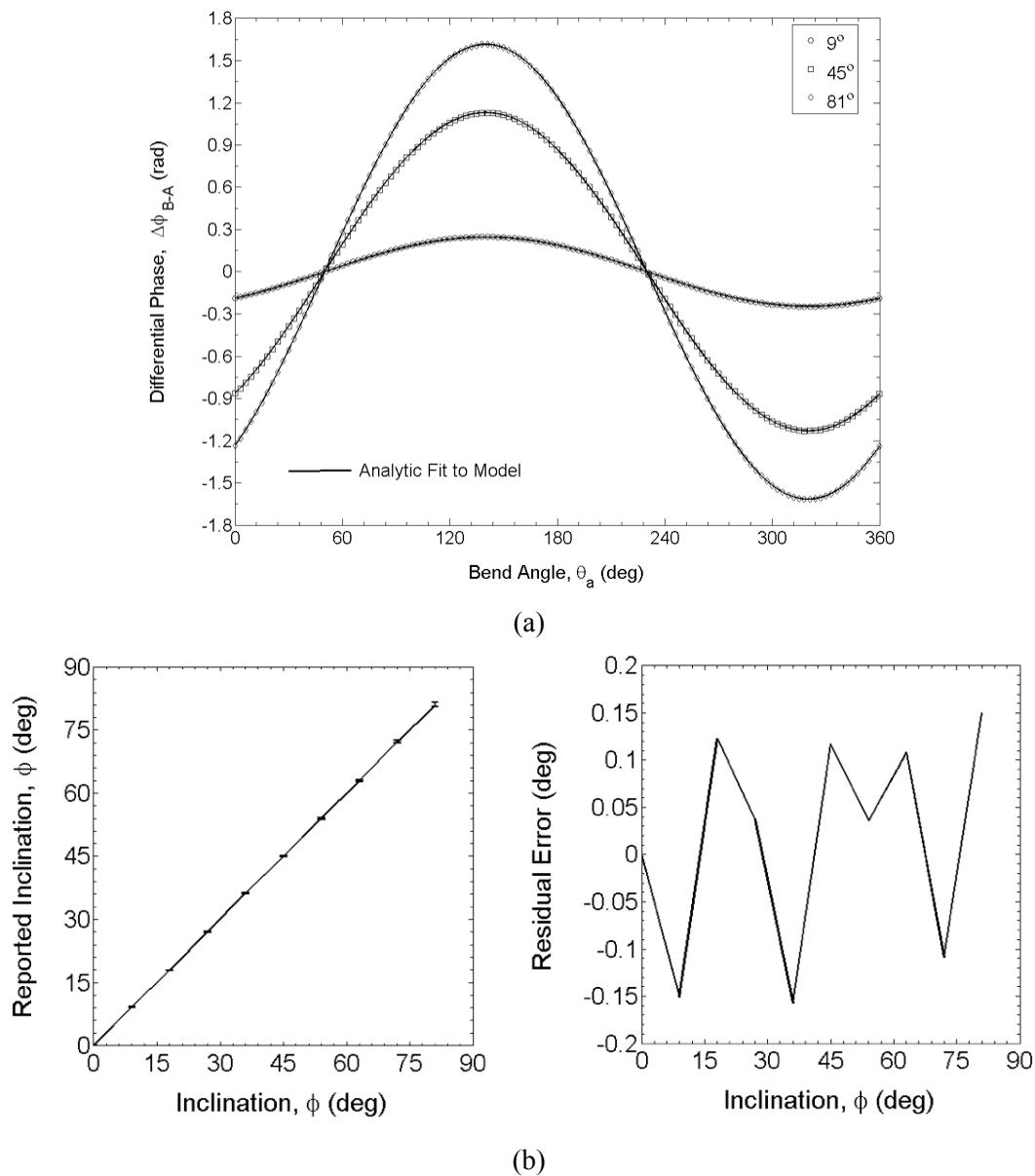


Fig. 10 – (a) Difference in strain between two cores as a function of rotation for difference inclinations and (b) reported inclination vs actual inclination for a bend angle of 120° and residual error

This sensor is a promising candidate to replace the MEMS inclinometer. It uses only single-mode fiber and thus can be operated over very large distances. Further development is required to miniaturize the optical interconnect between the MCF and single-core fibers used to interrogate the inclinometer as well as optimize the interferometric demodulator.

6. OPTICAL SYSTEM ARCHITECTURE FOR THREE-AXIS SENSOR SYSTEM

The optical architecture for a three-axis fiber laser magnetometer is an extension of the arrangement shown in Fig. 6(a) and is illustrated in Fig. 11. The pump power is supplied by two polarization multiplexed 980 nm laser diodes using a polarization maintaining combiner (PMC), which depolarizes the pump light.³ The pump light is delivered to the three laser sensors connected in series. A combined wavelength division multiplexer and isolator (ISO-WDM) is placed between each laser such that the light from each laser does not pass through the other lasers. This avoids generating optical feedback into the laser cavity, which can cause instability in the laser frequency. Each laser operates at a different wavelength, enabling them to be combined onto a single fiber and returned to the optoelectronic unit. Here they are passed through an imbalanced Michelson interferometer and separated with a wavelength division multiplexer before being detected.

The dither current for each sensor is generated using the technique described in Section 4. If the three sensors do not exhibit the same mechanical resonance frequency, then the dither signals for all three sensors can be combined. The resonant frequency of each sensor is determined by the tension applied to the ribbon, which can be adjusted during fabrication. The individual dither signals generated in Labview are summed and applied as a current modulation to the 1480 nm laser diodes. The dither current generated by the PPC in the sensing node is then injected into the bridge of all three magnetometers, which are also electrically connected in series. Since each sensor operates preferentially only at its specific resonant frequency and synchronous detection at this frequency is used to extract the magnetic field signal, the presence of other current modulation frequencies (such as the frequencies corresponding to the other two sensors and odd harmonic of all frequencies due to the square wave modulation) have no effect on the sensor signal response. This technique dramatically simplifies optical delivery of the dither current and requires only a single delivery fiber.

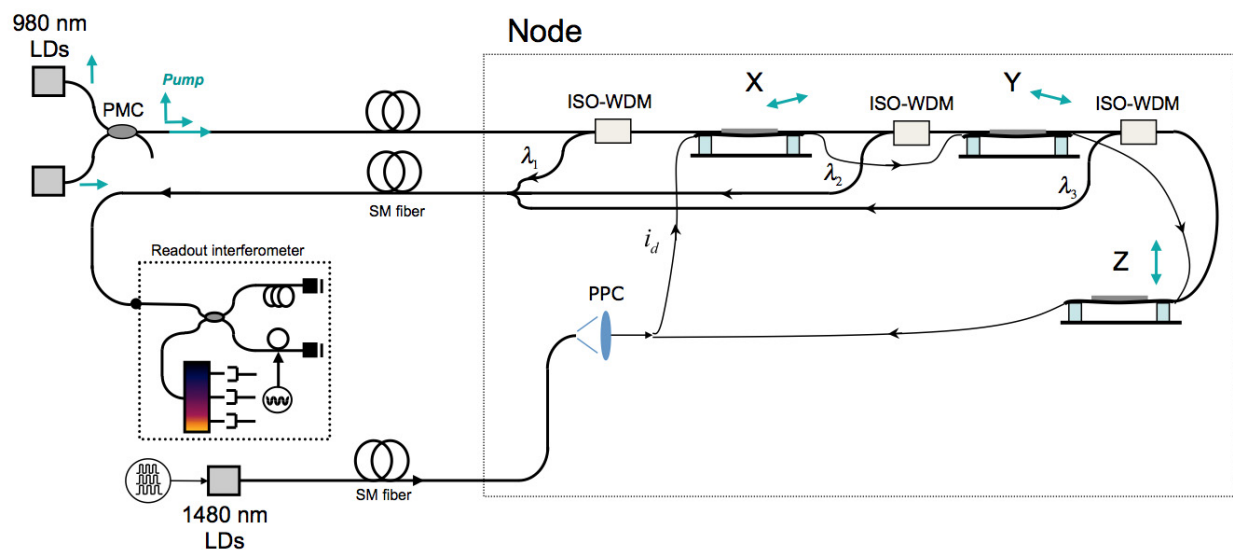


Fig. 11– Optical architecture of a three-axis magnetometer

³ Anisotropy of erbium ions in a silica host glass causes a polarization dependence of the absorption. This results in small fluctuations in the laser cavity temperature as the polarization of the pump changes. These temperature fluctuations both modulate the frequency of the laser and affect the thermal stability of the mechanical oscillator. Depolarization of the pump reduces these effects.

7. NODE DESIGN AND SENSOR INTEGRATION

A pressure-tolerant housing has been developed to accommodate three orthogonally mounted magnetometers and an inclinometer. A graphical illustration of the node layout is shown in Fig. 12(a) and the fully instrumented prototype node is shown in Fig. 12(b). The housing consists of an anodized aluminum base (pressure plate) with a milled circular recess. A fiber optic cable enters the base through a watertight feed-through. The cable is a commercially available fiber optic cable reinforced with Kevlar and carries 12 single-mode and 24 multimode optical fibers contained within gel filled tubes. The recess contains the PPC devices, splices and connectors. An instrumentation plate (platform) is fixed into the recess with vibration isolation mounts. These mounts provide inertial isolation of the magnetometers from motion of the base plate. Three magnetometers are mounted onto the instrumentation plate. The capacitor bank and MEMS inclinometer are also mounted alongside the magnetometers. Nonmagnetic materials (aluminum, titanium, brass, and acrylic) are used where possible to avoid introducing additional localized magnetic moments. A hemispherical acrylic dome is placed over the instrumentation plate and sealed with dual o-ring seals, providing a waterproof interface. This housing has been pressure tested to 100 m and is expected to survive at considerably higher depths. An additional polymer coating can be applied to the base material to prevent long-term corrosion. Four eye-bolts are located at the corners of the aluminum base enabling a rope to be used to lower the node to the seabed. The dimensions of the node are 303 mm × 303 mm × 180 mm (h).

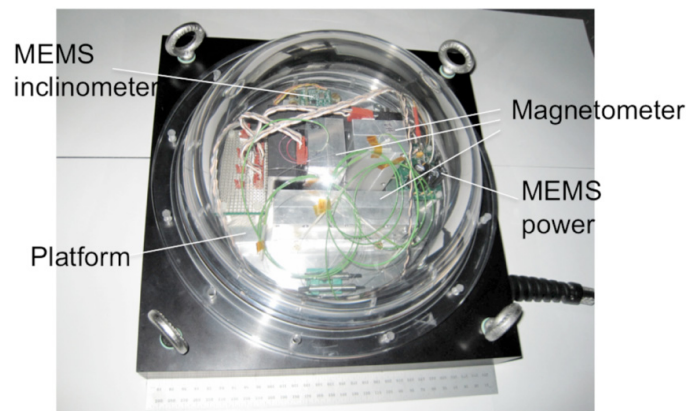
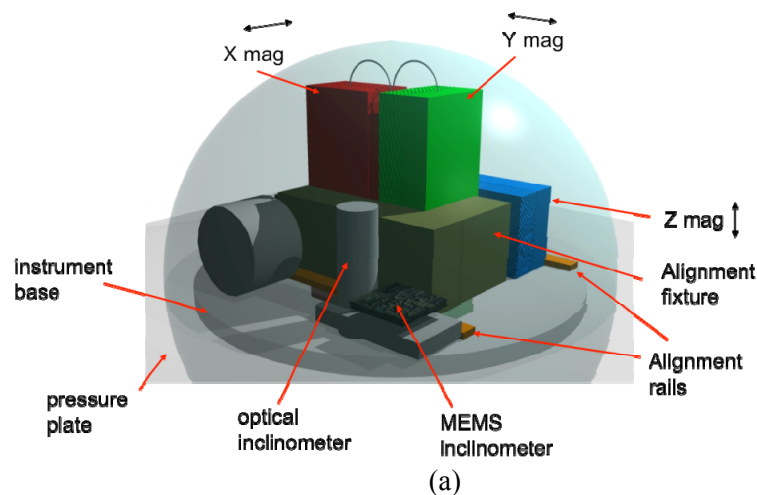


Fig. 12 – (a) Illustration of node layout and (b) fully instrumented node

8. PRELIMINARY SYSTEM EVALUATION AND FURTHER DEVELOPMENT

The basic operating principle of the node tethered with a 1 km undersea cable has been tested in the laboratory. Figure 13 shows the output of two orthogonal magnetometer axes aligned in a plane approximately parallel to the Earth's surface. The absolute measured levels reflect the local field experienced in the laboratory. The observed perturbations on this field correspond to a permanent magnet passing by the node. The characteristics of a moving dipole, resolved onto two orthogonal axes, are clearly visible in the measured data. This data is taken with the resonance locking method described in Section 3 activated. The update rate of the feedback circuit is approximately 1 Hz, limited by the processing speed of the quasi-realtime demodulator implemented in Labview. This update rate is insufficient to maintain operation at the resonant frequency in the presence of rapid changes in temperature (< 1 s) and thus introduces measurement error. This limitation can be overcome with a hardware implementation of the demodulator using a field programmable gate array (FPGA), which will permit greater than an order of magnitude increase in the locking bandwidth. Another source of long-term drift is due to temporal variation in the dither current amplitude. This can be overcome by maintaining a constant launch power for the optical dither signal through current feedback to the laser diode.

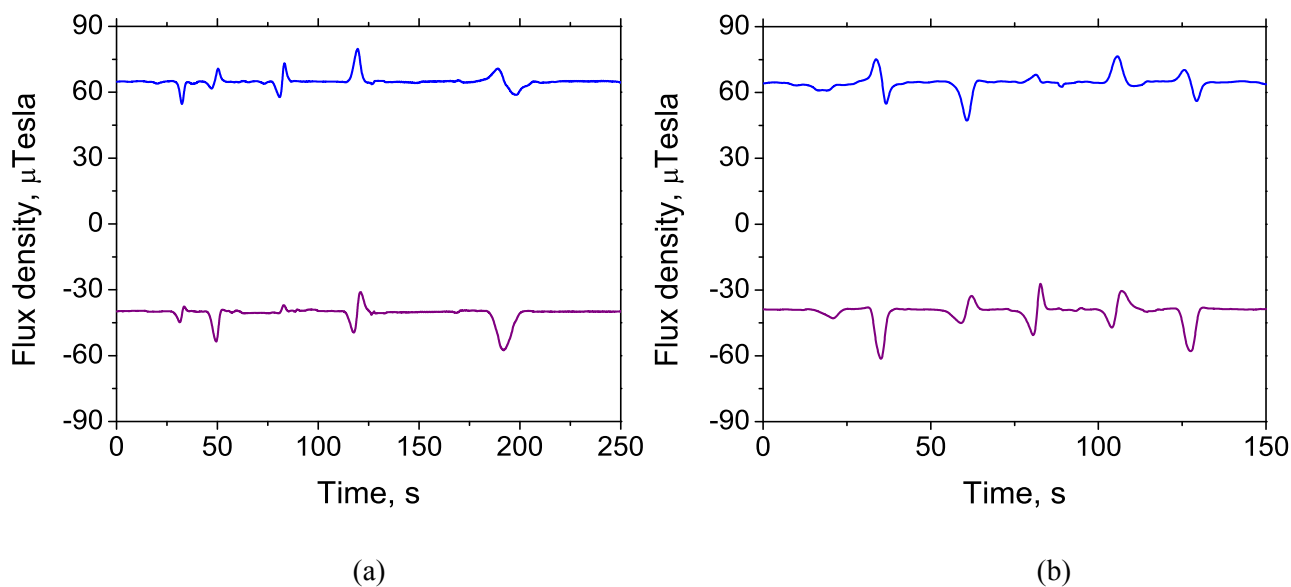


Fig. 13 – Response of two axes to passing magnetic dipole, (a) dataset 1 and (b) dataset 2

The dynamic range of the sensor is ~ 90 dB/Hz (dependent on the dither frequency) and is limited by the imbalance in the decoding interferometer and sampling rate of the demodulator. Optimization of the interferometer imbalance and investigation of other more bandwidth efficient demodulation techniques such as synthetic heterodyne, heterodyne or phase stepping are likely to improve the dynamic range by at least an order of magnitude.

The sensor system is designed to operate with a very large stand-off distance (e.g., greater than 10 km). The fiber laser sensor, when pumped at 1480 nm can operate over several tens of kilometers without degraded performance. In the current prototype, the standoff distance is limited by the attenuation of the multimode fiber (~ 3 dB/km) used to supply power to the MEMS inclinometer and to carry the MEMS signal back to the optoelectronics unit. At the time of development, it was not possible to obtain a VCSEL operating at 1310 nm or 1550 nm in single-mode fiber. However, these devices are likely to become

available in the near future. Also, a long wavelength version of the PPC configured for electrical power delivery is now available, enabling operation at 1480 nm in single-mode fiber.⁴ These upgrades will permit the use of single mode fiber in the low loss region of silica (1310 nm and 1550 nm) and reduce the attenuation to less than 0.4 dB/km, enabling the MEMS inclinometer to be operated over a larger distance.

Finally, it is appropriate to consider possible improvement in the performance of the magnetic field sensor. According to Eq. (2), the magnetic field resolution is limited by thermo-mechanical (TM) noise in the oscillator. The TM noise is inversely proportional to $Q^{1/2}$, thus increasing Q will increase the field resolution. However, it has also been shown that increasing Q also reduces the signal bandwidth. Thus, we can conclude that when operating at the fundamental limit, further improvement in signal resolution will come at the expense of a reduced signal bandwidth.

9. SUMMARY AND CONCLUSIONS

This report has described the development of a fiber optic, three-axis undersea magnetometer suitable for remote deployment. The transducer uses the Lorentz force acting on a current carrying bridge to modulate the emission frequency of a fiber laser strain sensor with magnetic field information. The laser frequency carries the magnetic field information back to an opto-electronic unit that can be located many kilometers from the sensor node. The sensor is shown to operate at its fundamental limit, due to thermo-mechanical noise, and is capable of achieving a magnetic field resolution of 343 pT/Hz^{1/2} at 1 Hz for 75 mA (rms) dither current when operated in a vacuum, over a measurement bandwidth of ~1 Hz. The dither current is generated by delivering a modulated optical signal to a custom designed photovoltaic power converter. This provides sufficient dither current to drive three magnetic field sensors. A pressure resistant housing has also been developed suitable for remote deployment. Three orthogonal magnetic field sensors are mounted onto an instrumentation plate contained within the housing. The inclination of the instrumentation plate is monitored with a MEMS based inclinometer, which is optically powered. The digital inclination signals are encoded onto an optical carrier by current modulating a VCSEL and transmitted back to the opto-electronics unit. The node is therefore electrically passive and connected only by an undersea fiber optic cable.

The key conclusions of this report are summarized below:

- A magnetic field sensor with fundamentally limited performance has been demonstrated to be capable of achieving a magnetic field resolution of 343 pT/Hz^{1/2} at 1 Hz for 75 mA (rms) dither current.
- Fiber laser sensor technology has been demonstrated as a highly effective method for measuring the oscillations of the bridge in each sensor and transmitting this information to a remote station.
- The deployable node is all-optical and can be interrogated over stand-off distances exceeding 10 km. This greatly exceeds the standoff distances achieved with other magnetic field sensing technology (i.e., flux-gate, fiber optic magnetostrictive).
- Inclination of the magnetometers is measured with an optically powered MEMS inclinometer. An all-optical inclinometer has been demonstrated as a potential replacement for the MEMS inclinometer.
- The undersea node contains little magnetic materials and is highly suited to long term monitoring applications.
- The reported system is suitable for integration with existing seabed mounted fiber optic hydrophone arrays, providing a combined magnetic and acoustic sensing capability with a common optical multiplexing architecture.

⁴ Part number PPC-9LW

- Future development of the system must focus on implementation of the demodulator in real time hardware, to provide the necessary resonance locking bandwidth. This will enable the long term drift of the sensor to be achieved.

10. ACKNOWLEDGMENTS

This program was funded from NRL 6.2 base funds and additional funds supplied by the Navy International Programs Office.

The authors would like to acknowledge C.G. Askins for developing the transducer design, node design and the soldering technique, R.E. Bartolo for investigating optical delivery of the dither and refining the soldering process, and J.R. Peele for early contributions to the transducer design.

REFERENCES

1. J. Watermann and J. Lam, "Distributions of Magnetic Field Variations, Differences and Residuals," SACLANTCEN Report SR-304, February 1999.
2. F. Bucholtz, C.A. Villaruel, A.R. Davis, C.K. Kirkendall, D.M. Dagenais, J.A. McVicker, S.S. Patrick, K.P. Koo, W. Gunnar, H. Valo, T. Lund, A.G. Andersen, R. Giessing, E.J. Eidem, and T. Knudsen, "Multichannel Fiber optic Magnetometer System for Undersea Measurements," *J. Lightw. Tech.* **13**(7), 1385-1395 (1995).
3. S. Søvik, "The Characterization and Recognition of Magnetic Disturbances Caused by the Movement of Vessels," SACLANTCEN Report IN-682, 1987.
4. D.M. Dagenais, F. Bucholtz, K.O. Koo, and A. Dandridge, "Demonstration of 3 pT/Hz^{1/2} at 10 Hz in a Fibre-Optic Magnetometer," *Elec. Lett.* **24**(23), 1422-1423 (1988).
5. A.D. Kersey, D.A. Jackson, and M. Corke, "Single-Mode Fibre Optic Magnetometer with DC Bias Field Stabilization," *J. Lightw. Technol.* **LT-3**(4), 836-840 (1985).
6. D.M. Dagenais and F. Bucholtz, "Measurement and Origin of Magnetostrictive Noise Limitation in Magnetic Fiber-optic Sensors," *Opt. Lett.* **19**(21), 1699-1701 (1994).
7. H. Okamura, "Fiberoptic Magnetic Sensor Utilizing the Lorentzian Force," *J. Lightwave Technol.* **8**, 1558-64 (1990).
8. R.B. Givens, J.C. Murphy, R. Osiander, T.J. Kistenmacher, and D.K. Wickenden, "A High Sensitivity, Wide Dynamic Range Magnetometer Designed on a Xylophone Resonator," *Appl. Phys. Lett.* **69**(18), 2755-2757 (1996).
9. G.A. Cranch, G.M.H. Flockhart, and C.K. Kirkendall, Proceedings of 18th Int. Conf. Opt. Fib. Sensors, OSA Tech. Digest, ISBN 1-55752-817-9, Cancun, Mexico, Oct. 23-27 (2006).
10. G.A. Cranch and G.M.H. Flockhart, "Fiber Laser Magnetic Field Sensor," U.S. patent application 20090102474, 2009.
11. G.A. Cranch, G.M.H. Flockhart, and C.K. Kirkendall, "High-resolution Distributed-feedback Fiber Laser DC Magnetometer Based on the Lorentzian Force," *Meas. Sci. Tech.* **20**, 034023 (2009).

12. J. Lübbe, L. Tröger, S. Torbrügge, R. Bechstein, C. Richter, A. Kühnle, and M. Reichling, "Achieving High Effective Q-factors in Ultra-high Vacuum Dynamic Force Microscopy," *Measurement Science and Technology* **21**(12), (2010).
13. J.E. Sader, "Frequency Response of Cantilever Beams Immersed in Viscous Fluids with Applications to the Atomic Force Microscope," *J. Applied Phys.* **84**(1), 64-76 (1998).
14. G.A. Cranch, C.G. Askins, R.E. Bartolo, G.A. Miller, and C.K. Kirkendall, "High Mechanical-Q Lorentz Force Sensor for DC Magnetic Field Measurement," Proceedings of SPIE 7503, paper 750330 (2009).
15. G.A. Cranch, G.M.H. Flockhart, and C.K. Kirkendall, "Distributed Feedback Fiber Laser Strain Sensors," *IEEE Sens.* **8**(7), 1161 (2008).
16. G.A. Cranch, G.A. Miller, C.G. Askins, and C.K. Kirkendall, "Characterization of a High Mechanical-Q Fiber Laser Lorentz Force dc Magnetometer," *Rev. Sci. Instr.* **82**(4), (2011).
17. A. Dandridge, A.B. Tveten, and T.G. Giallorenzi, "Homodyne Demodulation Scheme for Fiber Optic Sensors Using Phase Generated Carrier," *IEEE J. Quant. Elec.* **18**(10), 1647-1653 (1982).
18. G.A. Cranch, G.M.H. Flockhart, and C.K. Kirkendall, "Optically Powered DFB Fiber Laser Magnetometer," Proceedings of the 19th Int. Conf on Opt. Fiber Sensors, SPIE 7004, Perth, Australia, April 14-18 (2008).
19. G.M.H. Flockhart, G.A. Cranch, and C.K. Kirkendall, "Differential Phase Tracking Applied to Bragg Gratings in Multi-core Fibre for High Accuracy Curvature Measurement," *Electron Lett.* **42**(7), 390-391 (2006).
20. G.A. Miller, C.G. Askins, and G.A. Cranch, "Interferometric Interrogation of a Multicore Fiber, Two-axis Inclinometer," Proceedings of SPIE 7503, paper 75032R (2009).

APPENDIX

Derivation of the Signal Frequency Response

When the sensor is operated at its fundamental resonance, the signal frequency response can be determined using Eq. (7) by shifting the origin to the fundamental resonance, ω_r , such that,

$$|\hat{Z}(\omega_B)| = \left(\left[1 - \left(\frac{\omega_B + \omega_r}{\omega_r} \right)^2 \right]^2 + \frac{\left(\frac{\omega_B + \omega_r}{\omega_r} \right)^2}{Q^2} \right)^{-\frac{1}{2}}, \quad (\text{A1})$$

where ω_B is the angular frequency of the magnetic field. For the case when $Q \gg 1$ and $\omega_r \gg \omega_B$, Eq. (A1) reduces to

$$|\hat{Z}(\omega_B)| = Q \left(1 + \left(\frac{2Q\omega_B}{\omega_r} \right)^2 \right)^{-\frac{1}{2}}. \quad (\text{A2})$$

For static measurements, when $\omega_B \sim 0$, the normalized responsivity is equal to Q as expected. A corresponding expression for the phase can be derived using Eq. (8) to be

$$\phi(\omega_B) = -\pi / 2 - \tan^{-1} \left(\omega_r / (2Q\omega_B) \right). \quad (\text{A3})$$

For the case of a modulated magnetic field, the Lorentz force is expressed as

$$F_B(t) = B_0 \cos(\omega_B t) \cdot i_0 \cos(\omega_r t). \quad (\text{A4})$$

The laser frequency modulation can then be expressed as

$$\begin{aligned} \frac{\Delta v(t)}{v} &\propto B_0 i_0 \left(|\hat{Z}(\omega_B)| \cos((\omega_r + \omega_B)t + \phi(\omega_B)) + |\hat{Z}(-\omega_B)| \cos((\omega_r - \omega_B)t + \phi(-\omega_B)) \right) \\ &\propto B_0 i_0 |\hat{Z}(\omega_B)| \left(\cos((\omega_r + \omega_B)t + \phi(\omega_B)) + \cos((\omega_r - \omega_B)t - \phi(\omega_B)) \right) \end{aligned} \quad (\text{A5})$$

The interferometric decoder and demodulator converts this signal into an electronic signal of the same general form. The magnetic field signal is extracted by mixing it with the dither signal and low pass filtering to remove frequency components at $2\omega_r$, yielding

$$\frac{\Delta v(t)}{v} \propto B_0 i_0 |\hat{Z}(\omega_B)| \cos(\omega_B t + \phi(\omega_B)) \quad (\text{A6})$$

Thus, using Eqs. (A2), (A3), and (A6), the normalized signal frequency response can be expressed in complex form as

$$\hat{R}(f_B) = \left(1 + \left(\frac{2Qf_B}{f_2}\right)^2\right)^{-\frac{1}{2}} \exp\left(-i \cdot \tan^{-1}\left(\frac{f_r}{2Qf_B}\right)\right). \quad (\text{A7})$$